Single and Multipinhole Collimator Design Evaluation Method for Small Animal SPECT

Kathleen Vunckx[1], Dirk Bequé[1], Michel Defrise[2] and Johan Nuyts[1]

Abstract— **High resolution functional imaging of small animals is often obtained by single pinhole SPECT with circular orbit acquisition. Multipinhole SPECT adds information due to its improved sampling, and can improve the trade-off between resolution and sensitivity. To evaluate different pinhole collimator designs an efficient method is needed that quantifies the reconstruction image quality. In this paper, we propose a fast, approximate method that examines the quality of individual voxels of a post-smoothed MLEM reconstruction by studying their linearized local impulse response (LLIR) and (co)variance for a predefined target resolution. For validation, the contrast-to-noise ratios (CNRs) in some voxels of a homogeneous sphere and of a realistic rat brain software phantom were calculated for many single and multipinhole designs. A good agreement was observed between the CNRs obtained with the approximate method and those obtained with post-smoothed MLEM reconstructions of simulated noisy projections. This good agreement was quantified by a least squares fit through these results, which yielded a line with slope 1.02 (1.00 expected) and a y-intercept close to zero (0 expected). 95.4% of the validation points lie within three standard deviations from that line. Using the approximate method, the influence on the CNR of varying a parameter in realistic single and multipinhole designs was examined. The investigated parameters were the aperture diameter, the distance between the apertures and the axis-of-rotation, the focal distance, the acceptance angle, the position of the apertures, the focusing distance and the number of pinholes. The results can generally be explained by the change in sensitivity, the amount of post-smoothing and the amount of overlap in the projections. The method was applied to multipinhole designs with apertures focusing at a single point, but is also applicable to other designs.**

I. Introduction

Single pinhole collimated SPECT is regularly used nowadays for high resolution functional imaging of small animals. High resolution can be achieved, but the sensitivity is rather low and the data acquired with a circular orbit have been proven to be incomplete [1]. The use of a multipinhole collimator can increase the sensitivity without loss of resolution and the additional information can reduce the incompleteness. Mathematical analysis can only verify, however, whether the data are complete or not [1]. To be able to compare different single and multipinhole collimator designs a method is needed that quantifies how much information is missing. Pinhole collimator designs are usually compared based on their resolution and their sensitivity, calculated analytically, using Monte Carlo simulations or phantom measurements [2]–[6]. In this paper, we propose a new technique to evaluate single and multipinhole collimator designs with respect to the quality of each reconstructed voxel.

Quantifying the quality of a reconstructed voxel is typically done by exploring the properties of its linearized local impulse response (LLIR). In order to achieve a fixed (and more isotropic) target resolution for the LLIRs, we replace the usual maximum a posteriori (MAP) approach [7]–[10] by an efficient post-smoothed maximum likelihood expectation maximization (MLEM) approach. A similar, but slightly different approach, was proposed in [11], where a modified uniform Cramer-Rao bound with a resolution constraint was derived to be able to compare different multipinhole designs.

This paper is organized as follows. The new analytical pinhole collimator evaluation method, its usefulness and the reference method, used for the validation of the proposed efficient approximations, are explained in section II. Section III describes some simulation experiments. On the one hand, the experiments are meant to validate the new method. On the other hand, the influence of the most important design parameters on the image quality is investigated. First, some general parameters, such as the aperture diameter, are tested both for single and multipinhole designs. Second, the effects of multipinhole-specific design parameters are examined. The results of these experiments are presented in section IV and are further discussed in section V.

II. Theory

A. Linearized Local Impulse Response

For linear and shift-invariant imaging systems and reconstruction algorithms, the properties of the mean reconstruction image can be described by the (global) impulse response (in the spatial domain) or by the frequency response (in the Fourier domain). However, since the MLEM or MAP reconstruction $\hat{\Lambda}$ of the unknown activity distribution Λ for emission tomography is shift-variant and nonlinear in the projection data Q, an alternative approach is required. In [7] a generalization of the impulse response for emission tomography, called the

[1] K. Vunckx and J. Nuyts are with the Dept. of Nuclear Medicine, K.U.Leuven, B-3000 Leuven, Belgium. D. Bequé was with the Dept. of Nuclear Medicine, K.U.Leuven, B-3000 Leuven, Belgium. He is now with G.E. Global Research Europe, D-85748 Garching, Germany.

[2] M. Defrise is with the Dept. of Nuclear Medicine, V.U.Brussel, B-1090 Brussel, Belgium.

This work is supported by F.W.O. grant G.0174.03, K.U.Leuven grant IDO/02/012, I.W.T. grant SBO - ANIMONE and NIH GRANT R13 EB005531.

e-mail: kathleen.vunckx@uz.kuleuven.be

local impulse response (LIR) l^j has been proposed[1]:

$$l^j(\Lambda) = \lim_{\delta \to 0} \frac{\mu(\hat{\Lambda}(Q(\Lambda + \delta e^j))) - \mu(\hat{\Lambda}(Q(\Lambda)))}{\delta} = \frac{\partial}{\partial \lambda_j} \mu(\hat{\Lambda}) \quad (1)$$

where $\mu(x)$ denotes the mean of x, e^j is the j-th unit vector and j is the index of the voxel in the reconstructed image. The impulse response is local in two ways. First, due to the shift-variant character of the reconstruction and of the imaging system, the shape of the impulse response is a function of j. Second, it is object-dependent, or equivalently, nonlinear in the projection data, reflected by the argument Λ in equation (1).

To allow a more efficient calculation of the LIR, one can assume the reconstruction is locally linear [7]. Then the mean of many reconstructions of noisy projection data can be replaced by the reconstruction of noiseless projection data, as was experimentally confirmed by Wilson et al. [12]:

$$\mu(\hat{\Lambda}) \approx \hat{\Lambda}(\mu(Q(\Lambda))) \quad (2)$$

The substitution of (2) in (1) results in the following definition of the linearized local impulse (LLIR) [7]:

$$l^j(\Lambda) \approx \lim_{\delta \to 0} \frac{\hat{\Lambda}(\mu(Q(\Lambda + \delta e^j))) - \hat{\Lambda}(\mu(Q(\Lambda)))}{\delta} = \frac{\partial}{\partial \lambda_j} \hat{\Lambda}(\mu(Q(\Lambda))) \quad (3)$$

which will be taken as a starting point in this paper.

B. Reconstruction Quality Quantification

The goal of this paper is to find an efficient method that quantifies the image reconstruction quality induced by a single or multipinhole collimator design, such that many different designs can be compared quickly and easily. The properties of the LLIR, as described in the previous section, could - in principle - be used for this purpose.

The calculation of the LLIR and the (co)variance in a voxel using an iterative reconstruction algorithm and multiple noise realizations of the projection data, however, is very time-consuming. To calculate the LLIR in a voxel j, two reconstructions are required (one of the projection data of the object with an extra impulse in voxel j and one without impulse), as can be seen from equation (3). For each extra voxel that needs to be examined, an extra reconstruction is necessary. The computation of the covariance matrix of that voxel j involves the reconstruction of a large number x of noisy projection data sets. These data sets are obtained by computing x different Poison noise realizations of the simulated noise-free projection data of the phantom without impulse[2]. The relative error on the standard deviation is estimated to be $\sqrt{1/(2x)}$, assuming that the standard deviation is Gaussian distributed. This approach will be called the *reference method* in the rest of the paper.

Yet, optimizing the design of a multipinhole collimator for a specific application is practically infeasible using the reference method. Therefore, a much faster computational method is required. In [7], [9], [13] the following - more efficient - approximations for the LLIR and its covariance matrix after convergence of a MAP reconstruction have been formulated:

$$l^j(\Lambda) \approx [\boldsymbol{F} + \beta \boldsymbol{U}]^{-1} \boldsymbol{F} e^j \quad (4)$$

$$\mathrm{Cov}^j(\Lambda) \approx [\boldsymbol{F} + \beta \boldsymbol{U}]^{-1} \boldsymbol{F} [\boldsymbol{F} + \beta \boldsymbol{U}]^{-1} e^j \quad (5)$$

$$\text{with} \quad \boldsymbol{F} = \boldsymbol{A}^T \mathrm{diag}(\boldsymbol{Q})^{-1} \boldsymbol{A} \quad (6)$$

where $\boldsymbol{F}$ is the Fisher information matrix, which - in emission tomography - can be calculated by a projection $\boldsymbol{A}$, weighted by the projection data $\boldsymbol{Q}$ (where diag($\boldsymbol{Q}$) is a diagonal matrix with the elements of $\boldsymbol{Q}$ on the diagonal), and followed by a backprojection $\boldsymbol{A}^T$ (where ^{T} denotes transpose), β is the smoothing parameter and $\boldsymbol{U}$ is the Hessian of the quadratic prior, used for regularization.

The calculation of the LLIR in equation (4) requires the inversion of the JxJ matrix ($\boldsymbol{F}+\beta\boldsymbol{U}$), in which J represents the total number of image voxels. Given the relatively high number of image voxels in emission tomography, this solution is not feasible in practice. If $\boldsymbol{F}$ would be shift-invariant, however, it would be a circulant matrix (except for edge effects) and equations (4) and (5) would reduce to subsequent convolutions of the perturbation e^j with the convolution masks defined by $\boldsymbol{F}$ and $[\boldsymbol{F}+\beta\boldsymbol{U}]^{-1}$. Although single and multi-pinhole projections are not shift-invariant, and thus neither is $\boldsymbol{F}$, local shift-invariance could be assumed. This would only introduce a small error near the impulse in voxel j. This assumption has been proposed earlier in [9], [14] in the context of shift-variant PET, and in [10] for multipinhole SPECT. The Fisher information matrix $\boldsymbol{F}$ could then be approximated by a matrix $\boldsymbol{F}^j$ of which the rows are replaced by shifted versions of the j-th row. In this way $\boldsymbol{F}$ is turned into a circulant matrix $\boldsymbol{F}^j$ and the calculation of equations (4) and (5) can be done by convolutions in the spatial domain, as stated above, or by simple and even more efficient multiplications in the Fourier space.

To be able to easily compare different pinhole collimator designs, we choose to impose a fixed target resolution in the reconstruction image. For MAP reconstruction Stayman et al. [15] and Nuyts et al. [16] proposed methods that yield reconstructed images with isotropic, uniform resolution. Fessler [17] proposed a simpler analytical approach to get an isotropic spatial resolution. These methods are in fact equivalent to MLEM reconstruction run to convergence and post-smoothed to reach the imposed target resolution (see [15] for more details). Therefore we replaced the MAP regularization prior by a post-smooth filter $\boldsymbol{P}^j$ [18]. For each voxel j, this filter $\boldsymbol{P}^j$ is chosen to be the isotropic Gaussian that makes the approximation $\boldsymbol{T} \approx \boldsymbol{P}^j \boldsymbol{G}^j \boldsymbol{F}^j$ as accurate as possible, with $\boldsymbol{T}$ the isotropic Gaussian with a full-width at half-maximum (FWHM) equal to the target resolution and $\boldsymbol{G}^j$ the pseudoinverse of $\boldsymbol{F}^j$. The analytical approximations for the LLIR and the covariance of voxel j (in the spatial domain)

[1]The local impulse response l^j is a function of the voxel j, the unknown activity distribution Λ and the reconstruction algorithm. In order to keep the expressions readable, we limited the notation to $l^j(\Lambda)$.

[2]The (co)variance matrix for a voxel j is generally presumed to be equal for a phantom with and without impulse. This has as an advantage that these reconstructions (which are responsable for the main share of the computation time) can be reused for all voxels.

then become:

$$l^j(\Lambda) \approx \boldsymbol{P}^j \boldsymbol{G}^j \boldsymbol{F}^j e^j \quad (7)$$

$$\mathrm{Cov}^j(\Lambda) \approx \boldsymbol{P}^j \boldsymbol{G}^j \boldsymbol{F}^j \boldsymbol{G}^{jT} \boldsymbol{P}^j e^j \quad (8)$$

$$= \boldsymbol{P}^j \boldsymbol{G}^{jT} l^j(\Lambda) \quad (9)$$

We have slightly adapted the convolution mask represented by $\boldsymbol{F}^j$ in order to reduce the influence of the edge effects caused by the circulant approximation. This step was inspired by the triangular function proposed in the appendix of [19]. Approximations (7)-(9) predict very well the LLIR and covariance in voxel j close to this voxel, but become less accurate if the distance from j increases. Therefore, the elements of $\boldsymbol{F}^j$ are multiplied (in the spatial domain) by a weight that decreases with increasing distance from j. Empirically, the weight was set to one in voxel j and to zero at a distance from j equal to the number of columns in the reconstructed image. A linear decline was found to give accurate approximations.

In equations (7)-(9) matrix $\boldsymbol{G}^j$ represents an approximate pseudoinverse of matrix $\boldsymbol{F}^j$, since the inverse usually does not exist. Indeed, pinhole SPECT data acquisition is incomplete and $\boldsymbol{F}^j$ will therefore not be of full rank. In the MAP algorithm this is solved by adding a prior for regularization, as in equations (4) and (5). For MLEM we propose the following approximation $\mathbf{G}^j$ of the pseudoinverse (in the Fourier domain):

$$\mathbf{G}^j = \frac{\mathbf{F}^{j*} \max\left(\Re(\mathbf{F}^j), 0\right)}{\mathbf{F}^{j*}\mathbf{F}^j \max\left(\Re(\mathbf{F}^j), 0\right) + \epsilon} \quad (10)$$

with $\mathbf{G}^j$ and $\mathbf{F}^j$ the Fourier transform[3] of $\boldsymbol{G}^j$ and $\boldsymbol{F}^j$, respectively, * the complex conjugate, $\Re(\mathbf{F}^j)$ the real part[4] of $\mathbf{F}^j$ and $\epsilon = 10^{-10}|\mathbf{F}^j_{DC}|^3$, where $\mathbf{F}^j_{DC}$ denotes the DC-value of $\mathbf{F}^j$ in the Fourier domain, or the mean value of the corresponding image in the spatial domain. Regularizing effects were obtained by removing the negative frequencies and by choosing an appropriate ϵ.

As measures for the reconstruction quality in voxel j the contrast recovery coefficient (CRC) and the variance of the LLIR in voxel j (which are the j-th element of l^j and Cov^j, respectively) are commonly used. The CRC can be seen as a measure of resolution [8]. Thanks to the fixed resolution after post-smoothing, the CRC should be more or less constant. The only parameter to optimize then is the variance. As an alternative the contrast-to-noise ratio (CNR) can be optimized as well, since

$$\mathrm{CNR} = \frac{\mathrm{CRC}}{\sqrt{\mathrm{variance}}}. \quad (11)$$

In the rest of this paper the CNR is taken as the image quality measure.

C. Collimator Design Parameters

When designing a single pinhole collimator, only a few parameters have to be taken into consideration, namely:

- The aperture diameter (D).
- The distance between the aperture and the axis-of-rotation (AOR), abbreviated as DA.
- The distance between the aperture and the detector (DD), also called focal distance.
- The aperture acceptance angle (A).
- The pinhole aperture plate thickness (T).
- The linear attenuation coefficient of the pinhole aperture plate, depending on the material (usually tungsten) and the energy of the isotope used.

These will be called the *general pinhole design parameters* in the rest of this paper.

The addition of pinhole apertures, however, causes a dramatic increase in the collimator design complexity. Extra parameters are:

- The position of the aperture (in polar coordinates) with relation to the other apertures (PD and PA, see figure 1).
- The focusing distance (F), which is the distance between the apertures and the point at which the apertures focus (i.e. the point where the central axes of the apertures intersect each other).

This second group of parameters are *multipinhole-specific design parameters*. Remark that, in this paper, we force all apertures to focus at one point (on the central axis of the central pinhole), since we are only interested in imaging a small region (e.g. the brain), not the whole body. This means that the inclination angle I of each aperture can be derived from the focusing distance F and the position of the aperture (PD and PA). If the apertures would not focus all at the same point, two additional parameters for each aperture - instead of the fixed focusing distance F - would be necessary to specify the geometry of the design uniquely.

All above described parameters, except for the aperture diameter, are visualized in figure 1.

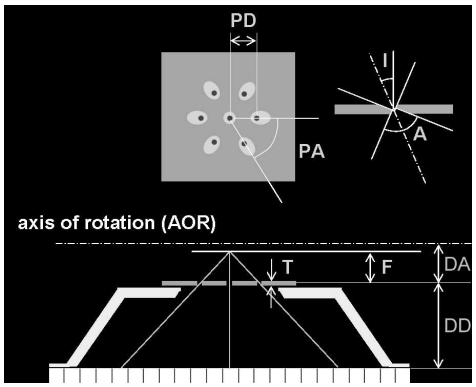

Fig. 1. Illustration of the pinhole collimator design parameters.

To reduce the complexity of the multipinhole designs, we restrict the apertures (a) to lie in the same plane parallel to the detector (which is supposed to be parallel to the AOR), (b) to focus at one point (i.e. the image center if not specified otherwise), and (c) to form a regular polygon around a central pinhole. In addition, the parameters D, A and T are chosen equal for all pinhole apertures. Of course, it is possible that

[3]Before performing the Fourier transform (and the above mentioned weighting) the image is zero padded.

[4]Note that, for the calculation of $\Re(\mathbf{F}^j)$, the image has to be shifted before Fourier transformation, such that the DC-value is located at [0, 0, 0].

other designs result in a better reconstruction quality, but this is beyond the scope of this work.

III. Experiments

The rationale of the experiments presented in this paper is twofold. On the one hand, these experiments are meant to validate the proposed approximations for the CRC and the variance, which are presumed to quantify the image quality, for various single and multipinhole collimator designs (section III-A). On the other hand, the experiments are set up to examine the influence of the different design parameters on the reconstruction image quality, by varying one parameter while keeping all others fixed (section III-B).

A. Validation of the Approximate Image Quality Quantification Method

Some efficient approximations to calculate the LLIR and its covariance in an image voxel j were proposed in section II-B. Before these analytical approximations can be applied routinely to evaluate and optimize single and multipinhole designs, they should be validated with respect to the reference method, based on post-smoothed MLEM iterative reconstructions (see section II-B for more details on the reference method).

Many different designs (see section III-B) were simulated and tested for their corresponding image quality. A subset of the experiments presented in this paper was performed twice: once using the approximate method (equations (7)-(10)) and once more - for validation - with the reference method. For each validation experiment, the outcome of both methods will be compared and discussed in section IV. Many designs were validated to be sure the approximate method was not only valid (by chance) for a specific test design.

Two different software phantoms, a homogeneous sphere and a rat brain phantom (see figure 2), were used in the experiments to show that the new method is accurate independently of the imaged object. Although the method was mainly tested for a homogeneous sphere, it should be valid for any object.

The homogeneous sphere had a radius of 17.5 mm and was simulated in an image space with 65x65x65 cubic voxels of 0.8 mm. The activity in the sphere was set to 5 kBq/mm^3. A coronal slice of this sphere is shown in figure 2(a) and the six investigated voxels are pointed out with a number. To avoid overloading the graphs, only the results of the three most extreme voxels (indicated with a diamond, a triangle and a rectangle (points 1, 3 and 6, respectively)) are shown in sections IV-A and IV-B. In section IV-C the results of all six voxels are plotted.

The rat brain phantom has been built based on the reconstruction of a real rat brain measurement with ^{123}I-FP-CIT to visualize the striata (as in [23]). This three-dimensional image was thresholded to segment it into regions with similar activity uptake. These regions are (in order of increasing uptake): the body of the rat, the brain, the striata in the brain, the glands behind the eyes, called Harderian glands, and the salivary gland (outer and inner region). The body was filled with a homogeneous background activity, although in reality there is not uptake everywhere. All segments contained realistic amounts of activity. Again an image space with 65x65x65 cubic voxels of 0.8 mm was simulated. A transaxial, coronal and sagittal slice of the software phantom are shown in figure 2(b)-2(d). The same voxels as for the homogeneous sphere were considered.

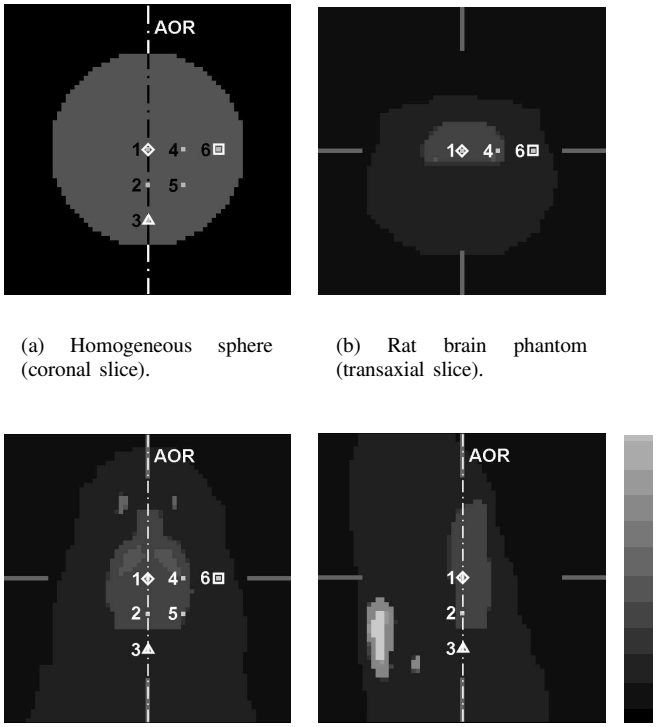

(a) Homogeneous sphere (coronal slice).

(b) Rat brain phantom (transaxial slice).

(c) Rat brain phantom (coronal slice).

(d) Rat brain phantom (sagittal slice).

Fig. 2. Illustration of the homogeneous sphere (coronal slice) and the rat brain phantom (transaxial, coronal and sagittal slice). The examined voxels where depicted.

Both the approximate and the reference method start from a simulated forward projection of the activity in the chosen software phantom (with or without an impulse in the voxel of interest) onto the detector, which is assumed to be an infinitely thin, perfect absorber with an intrinsic resolution of 4 mm. The projection method defines for each detector pixel and for each aperture a cone through the field of view (FOV) which contains all voxels that contribute to the intensity measurement of that pixel. The contribution of each voxel is weighted by a factor, which depends on the distance between the voxel and the detector. These weights are calculated once beforehand, and are used for all forward and backward projections in the approximate, as well as in the reference method. In this way, the resolution and sensitivity of the pinhole apertures are modeled. However, our current implementation of the projection method does not allow edge penetration modeling yet. Effects due to scatter and attenuation were neglected.

For the reference method, a series of independent noise realizations was computed using a pseudo-random Poisson noise generator. The sets of noisy data were reconstructed

using MLEM with relaxed ordered subsets (OS) [20]–[22]. An equivalent of 472 MLEM iterations were performed, to reach an estimate near convergence. The reconstructed images were post-smoothed in order to obtain a resolution of 2.4 mm FWHM in the voxel of interest. The calculation of the variance (using the reference method) was based on 150-300 noise realizations[5].

B. Effect of Pinhole Collimator Design Parameters

The presented method will be useful in many ways. Our two main purposes are: (a) to gain insight in the influence of the different design parameters on the image quality, and (b) to optimize the collimator design for specific applications. The former will be elaborated in more detail in this section, and will be useful for the latter, the design phase, which is subject of ongoing research in our lab.

To examine the effect of the different pinhole design parameters, we started for each experiment from the same realistic single pinhole design or from one of two realistic multipinhole designs. While keeping all other parameters fixed, the parameter of interest was varied. We investigated the following parameters: the aperture diameter (D), the distance between the pinholes and the AOR (DA), the focal distance (DD), the acceptance angle (A), the distance between the central aperture and the surrounding ones (PD), the focusing distance (F) and the number of pinhole apertures (NP). The first 4 parameters, the *general pinhole design parameters*, were both investigated for single and multipinhole designs. The last 3 parameters are only applicable to multipinhole designs. They were categorized under the name *multipinhole-specific design parameters*.

1) Fixed parameters: Since at our lab we focus on rat brain imaging using a Siemens E.cam camera, we fix the parameters to realistic values as well for the pinhole collimator design as for the camera parameters and the phantom size. In this work we use only one of the two detector heads, since the reference method is very time-consuming and the extension from one to more detector heads is straightforward and has no influence on the accuracy of the approximate method.

The simulated SPECT scanner acquired the data in a 256x200 matrix with square pixels of 1.95 mm. The intrinsic resolution of the detector was 4.0 mm FWHM. The distance between the detector and the AOR was 218 mm. A perfect circular orbit with 64 equally spaced projection angles was assumed. Each projection image was acquired in 60 s.

The pinhole collimator design was inspired by and very similar to the design proposed by Schramm in [3]. It consists of a lead pyramid with a tungsten pinhole insert plate (thickness 12 mm) on top of it. The knife-edge pinhole aperture of the single pinhole design was positioned centrally with respect to the detector at a focal distance of 173 mm. The aperture had a diameter of 1.5 mm, an acceptance angle of 60° and its central axis was perpendicular to the detector plane.

Two different multipinhole collimator designs were taken as a starting point for the experiments. To image the homogeneous sphere, a 7-pinhole collimator was simulated. Six pinholes were uniformly distributed over a circle with a radius PD of 25 mm around the central aperture. In the rest of this paper this radius will be called the *pinradius*. Three apertures were located on a line parallel to the AOR. All pinholes had an aperture diameter of 1.2 mm, an acceptance angle of 60°, and focused at a point at 45 mm from the central one (i.e. at the image center). These parameters were chosen because they result in a good detector filling with modest overlap between the projections through the different apertures.

To reduce the simulation time for the validations, the rat brain phantom was imaged with a pinhole collimator with only 4 apertures, one central and three on the vertices of a regular triangle. Again a pinradius of 25 mm was chosen. One of the outer apertures was positioned on the line through the central pinhole and parallel to the AOR. The aperture diameter was taken 1.5 mm. The rest of the design parameters were equal to those of the 7-pinhole collimator.

A summary of the three above specified pinhole designs can be found in table I.

TABLE I
MAIN PINHOLE COLLIMATOR DESIGN PARAMETERS

	1-pinhole	4-pinhole	7-pinhole
D	1.5 mm	1.5 mm	1.2 mm
DA	45 mm	45 mm	45 mm
DD	173 mm	173 mm	173 mm
A	60°	60°	60°
PD		25 mm	25 mm
F		45 mm	45 mm

2) Varying parameters: As explained earlier in this section all design parameters were kept fixed, except one. For the global pinhole design parameters D, DA, DD and A, both a single and a multipinhole experiment was performed. First, the diameter D was varied from 0.6 to 2.4 mm with an interval of 0.3 mm. Second, distances between the apertures and the AOR (DA) from 30 to 60 mm, in steps of 5 mm, were considered. Third, the focal distance was varied from 113 to 233 mm in steps of 20 mm. Fourth, the acceptance angle was changed from 20° to 80° with intervals of 10°.

For the multipinhole-specific design parameters several multipinhole designs were tested. First, the pinradius was increased from 15 to 45 mm in steps of 5 mm. Next, the focusing distance was varied from 30 to 60 mm with an interval of 5 mm. Finally, designs with 5 to 13 pinholes were compared.

An overview of the experiments is given in table II. As can be seen from the penultimate column, the homogeneous sphere and the rat phantom were used alternatingly in the experiments.

IV. RESULTS

In sections IV-A and IV-B, the results of many different pinhole designs, evaluated with the presented approximate method, are shown and discussed. For validation, part of these designs were evaluated with the reference method as well. In section IV-C, all validation points are gathered to get a global overview of the agreement between the new method and the reference method.

[5]Due to the very long calculation time of the reference method, only for a small part of the designs more than 150 noise realizations were performed.

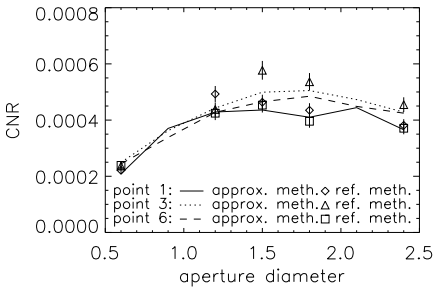

(a) Diameter vs CNR (sphere, 1 pinhole)

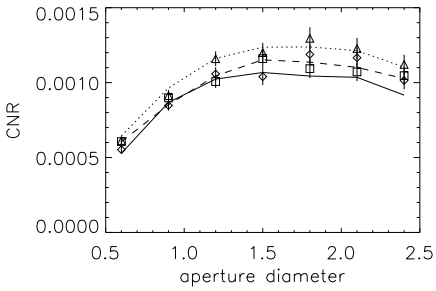

(b) Diameter vs CNR (sphere, 7 pinholes)

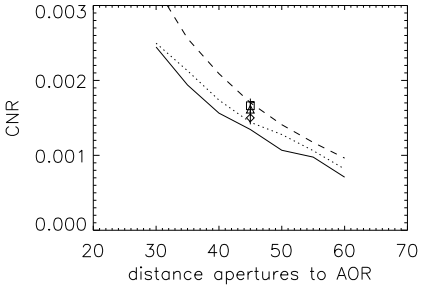

(c) Distance apertures to AOR vs CNR (rat, 1 pinhole, D=1.5 mm)

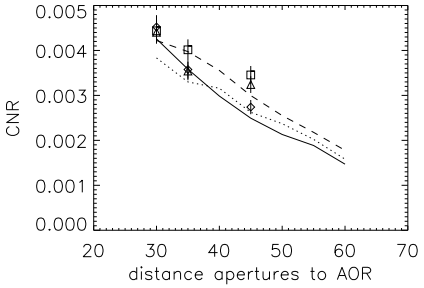

(d) Distance apertures to AOR vs CNR (rat, 4 pinholes, D=1.5 mm)

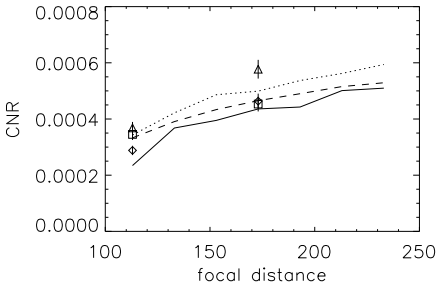

(e) Focal distance vs CNR (sphere, 1 pinhole, D=1.5 mm)

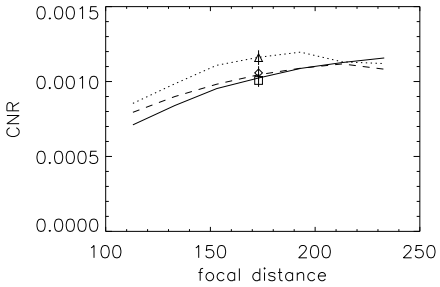

(f) Focal distance vs CNR (sphere, 7 pinholes, D=1.2 mm)

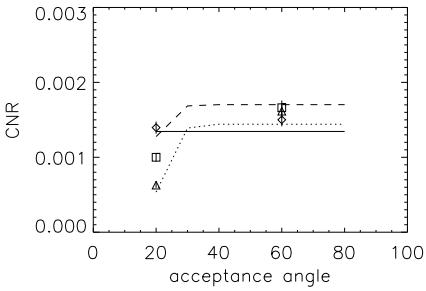

(g) Acceptance angle vs CNR (rat, 1 pinhole, D=1.5 mm)

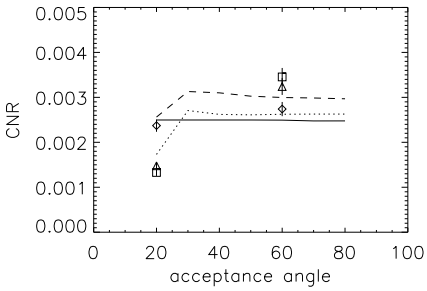

(h) Acceptance angle vs CNR (rat, 4 pinholes, D=1.5 mm)

Fig. 3. Evaluation of the influence of the different global pinhole design parameters on the reconstruction quality of a homogeneous sphere or a rat brain phantom. Left: single pinhole designs, right: multipinhole designs. The error bars indicate one standard deviation. The target resolution was 2.4 mm.

TABLE II

VARYING PINHOLE COLLIMATOR DESIGN PARAMETERS

	Interval	Step	Phantom	Starting design
D	0.6-2.4 mm	0.3 mm	sphere	1-pinh. and 7-pinh.
DA	30-60 mm	5 mm	rat	1-pinh. and 4-pinh.
DD	113-233 mm	20 mm	sphere	1-pinh. and 7-pinh.
A	20°-80°	10°	rat	1-pinh. and 4-pinh.
PD	15-45 mm	5 mm	sphere	7-pinhole
F	30-60 mm	5 mm	rat	4-pinhole
NP	5-13 pinh.	1 pinh.	sphere	7-pinhole

A. *Effect of General Pinhole Design Parameters*

1) Aperture Diameter (D): For the single and multipinhole SPECT setups (with an aperture diameter between 0.6 mm and 2.4 mm), the reconstruction image quality in three voxels of the homogeneous sphere (see figure 2(a) points 1, 3 and 6) are displayed in figures 3(a) and 3(b) respectively. The solid, dotted and dashed line connect the results for point 1, 3 and 6, respectively, obtained with the approximate method. The results acquired with the reference method are displayed as diamonds, triangles and rectangles for point 1, 3 and 6, respectively.

Figures 3(a) and 3(b) show that, for a target resolution of 2.4 mm, the CNR reaches a (rather flat) maximum at an aperture diameter of about 1.5-1.8 mm. The results show a very similar behavior for single and multipinhole collimators, but the CNR is much higher with the multipinhole design, as expected. The graphs also reveal good agreement between the analytical prediction and the reference method.

Two complementary effects contribute to variance reduction. First, increasing the aperture diameter leads to increased sensitivity and hence reduced variance. Second, post-smoothing the MLEM reconstruction reduces the variance as well. Apparently, the optimal variance reduction is obtained with a combination of both contributions. When the aperture diameter is further increased, the corresponding reduction of the post-smoothing (required to reach the target resolution) leads to a net increase of the variance. Similar findings were reported by Fessler [24]. In addition, as the optimum is relatively flat, it might be interesting to take a slightly larger aperture diameter in order to reduce the influence of collimator scatter.

2) Distance Apertures to AOR (DA): Decreasing the distance between the aperture(s) and the rotation axis should lead to improved resolution and sensitivity. Because the resolution is kept constant at the target resolution by post-smoothing, the CNR is expected to increase due to a reduction of the variance. This is confirmed by figures 3(c) and 3(d).

For the points studied in the rat phantom, the distance DA can be reduced until the aperture plate touches the phantom without noticeable degrading effects due to truncation of projections. To illustrate the effect of truncation, the experiments were repeated with a reduced acceptance angle (40° instead of 60°). As shown in figures 4(a) and 4(b), the reduction of the FOV and the according increase in truncation now limit the increase of the CNR at small distances for the eccentric points (numbers 3 and 6).

As shown in figure 3(d), three multipinhole designs were validated. The approximations again agree very well with the

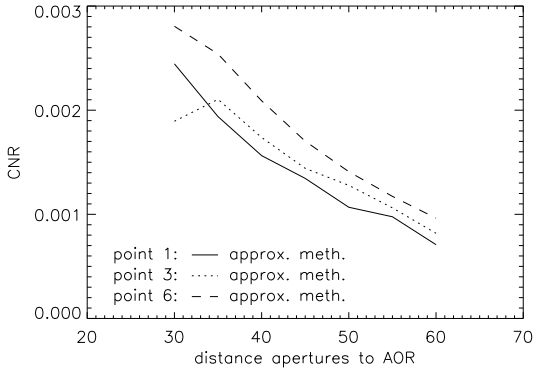

(a) Dist. apertures to AOR vs CNR (rat, 1 pinhole, D=1.5 mm, A=40°)

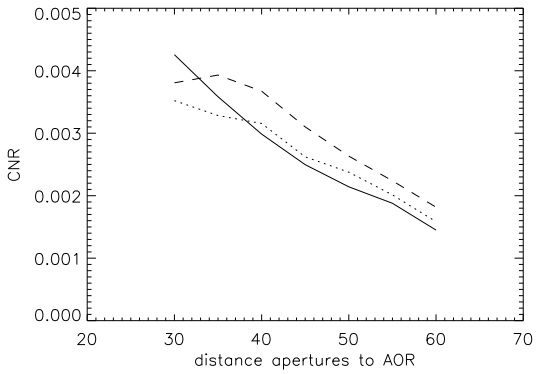

(b) Dist. apertures to AOR vs CNR (rat, 4 pinholes, D=1.5 mm, A=40°)

Fig. 4. Illustration of the reduction of the image quality (in points 3 and 6) due to the truncation effect in case of a small distance between the apertures and the AOR (DA=30 mm) and a small acceptance angle (A=40°). Top: single pinhole designs, bottom: multipinhole designs.

results obtained with the post-smoothed MLEM reconstructions. As in the previous experiment, the CNR is higher for the multipinhole designs because of the three extra apertures.

3) Focal Distance (DD): Varying the focal distance modifies the magnification, but has little influence on the sensitivity. This is in contrast with the previous parameter (DA), which strongly influences the sensitivity. This difference between the two parameters explains the observation that the CNR varies more slowly when varying DD (see figures 3(e) and 3(f)) than when varying DA, as in figures 3(c) and 3(d).

For the single and multipinhole designs the same trends are found. Though, one should note that for multipinhole designs with a very large focal distance the quality of the eccentric points starts to degrade. The cause is twofold. On the one hand, the large magnification, induced by the large focal distance, results in overlapping projections to which the eccentric points are more susceptible than the central points. For a detector pixel gathering activity from more than one aperture, i.e. for

a pixel in a region of overlap, uncertainty about the origin is introduced and the photon count will be worth less than in the case without overlap. On the other hand, the magnification can cause projection truncation. If a voxel is seen through less apertures, its image quality is obviously degraded.

Two single pinhole designs were validated as can be seen in figure 3(e). The CNRs obtained with the reference method confirm those calculated with the new efficient method.

4) Acceptance Angle (A): To test the influence of the acceptance angle on the image quality, we varied the angle between 20° and 80°. The rat phantom was used in the simulations.

From the results, shown in figures 3(g) and 3(h), we can conclude that for the investigated voxels in the rat phantom - given the current design parameters - an acceptance angle of 40° is sufficiently large. Further reduction of the acceptance angle leads to loss of information in the eccentric voxels, due to the reduced FOV. Enlarging the acceptance angle might be interesting if one would like to scan also larger animals with the design, or if larger parts of the animal are of interest.

Increasing the acceptance angle in multipinhole designs increases the amount of overlap between the projections acquired through different pinholes. This results in a slight decrease of the CNR (see figure 3(h)).

For both experiments two designs were validated. The approximate method again predicted well the CNRs found with the reference method.

Note that in figure 3 the CNR for point 1 is generally lower than the CNR for points 3 and 6. This can intuitively be explained as follows. Because of its central location in the phantom (both in the sphere and in the rat brain phantom), any line of response (LOR) through voxel 1 also contains many other high intensity voxels. As a result, all information about voxel 1 is superimposed on a high intensity 'background' from the other contributing voxels. The contribution of voxel 1 to these measurements is therefore hardly separable from the measurement noise, resulting in a high variance for voxel 1. As voxels 3 and 6 generally have less intense voxels on their LORs, their variance is lower compared to the variance for voxel 1. This can also be verified with equations (6), (9), (10) and (11), which confirm that the CNR decreases for increasing count $\boldsymbol{Q}$.

B. Effect of Multipinhole-Specific Design Parameters

1) Pinradius (PD): Predicting the effect of changing the distance between the central and the surrounding apertures is very difficult, because the image quality is affected by many counteracting influences. First, as the pinradius increases, the sensitivity drops, because the (mean) distance from a random voxel to the pinhole apertures increases. This induces obviously a decrease in image quality in that voxel. Second, the amount of overlap between the projection images, and thus also the number of voxels that are projected onto the detector in an overlap region, reduces with a growing pinradius, which should be beneficial. Third, an increasing pinradius causes the projections of a voxel to move outward. Therefore some projections might fall outside the detector area, again reducing the CNR.

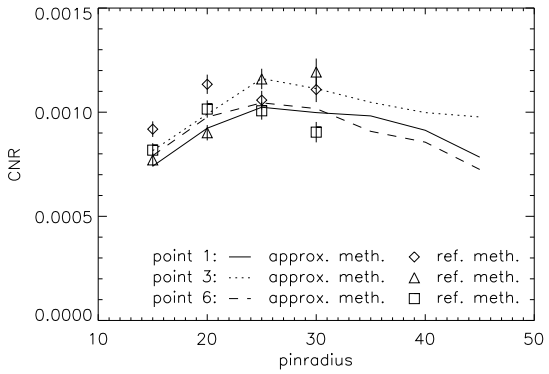

(a) Pinradius vs CNR (sphere, 7 pinholes, D=1.2 mm)

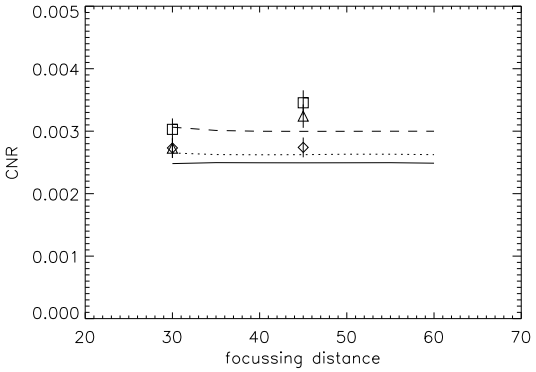

(b) Focusing distance vs CNR (rat, 4 pinholes, D=1.5 mm)

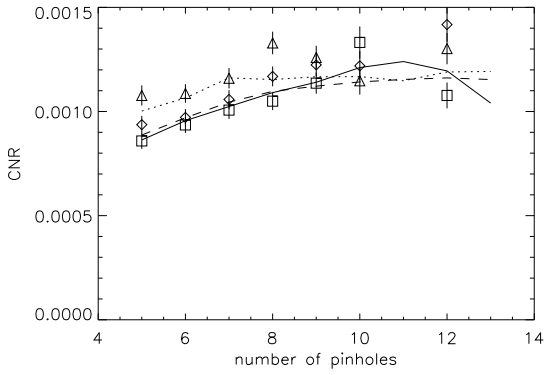

(c) Number of pinholes vs CNR (sphere, 5-13 pinholes, D=1.2 mm)

Fig. 5. Evaluation of the influence of the different multipinhole-specific design parameters on the reconstruction quality of a homogeneous sphere or a rat brain phantom. The error bars indicate one standard deviation. The target resolution was 2.4 mm.

In this paper, the reconstruction quality is evaluated in each individual voxel. Therefore, the effect of the change in pinradius, and thus also the effect of the above mentioned

influences, is examined for each voxel of interest separately. For this reason we studied the behaviour of the projections of the activity in the voxel of interest through the different apertures, while changing parameter PD.

All investigated voxels in the homogeneous sphere reach their maximum image quality at a pinradius of 25 mm (see figure 5(a)). However, these points experience the increase in distance between the apertures very differently. The projections of the central voxel (point 1) start to overlap with other projections for a pinradius of 20 mm. Projection truncation begins at 40-45 mm. Therefore, below 20 mm and above 40 mm the quality is expected to decrease rapidly. The slight decrease in between (see solid line in figure 5(a)) can be explained by the reduction in sensitivity. The eccentric voxel on the AOR (point 3) suffers already from overlap at a pinradius of 25 mm and some projections of the point start to fall outside the detector area from a PD of 30-35 mm. The optimum (see dotted line in figure 5(a)) is, as expected, more clear. The eccentric point in the central plane (point 6) is not influenced by any overlap any more at a PD of 35 mm, but from a PD of 30-35 mm the information drops due to truncated projections. Figure 5(a) (dashed line) suggests that for this voxel the higher sensitivity for designs with a PD of 25 or 30 mm manages to compensate for the deteriorating influence of the overlap.

The four designs with the smallest pinradius were successfully validated with the reference method.

2) Focusing Distance (F): From figure 5(b), it can be concluded that the effect of the focusing distance on the reconstruction quality of the rat brain phantom is negligible. This is due to the fact that the acceptance angle is still large enough to cover the investigated points.

The two validated designs gave satisfactory results.

3) Number of Pinholes: The effect of the addition of pinholes can be studied from figure 5(c). As expected, at first the CNR increases with the number of pinhole apertures thanks to the increased sensitivity. However, due to overlap, the extra sensitivity does not simply stand for increased information and a saturation point will be reached, as was also observed by Cao et al. [6]. For the central voxel (point 1) the image quality is best for 11 apertures. Adding more pinholes reduces the CNR. The axially eccentric voxel (point 3) does not benefit from using more than 7 apertures. However, this does not degrade the image quality either. For the eccentric voxel in the central plane (point 6) the curve starts flattening around 9 pinholes.

For most designs the CNR was also calculated using the reference method. Most predictions match well with the validation results. The latter show the above discerned trends less clearly due to noise. For the first 5 designs between 250 and 300 noise realizations were simulated instead of 150, hence their shorter error bars.

C. Method Validation: Overview

All validation points are shown in one graph (see figure 6(a)), which plots the CNR calculated with MLEM reconstructions with respect to the predicted CNR. The solid line was fitted to minimize the least squares distance to these points. The dashed lines indicate distances of one and two standard deviations from the fitted line. The standard deviation on the CNR could be found from the relative standard deviation on the variance, since the CRC was calculated from noiseless data. Hence, for most points the relative standard deviation on the CNR is $\sqrt{1/(2*150)} = 0.058$.

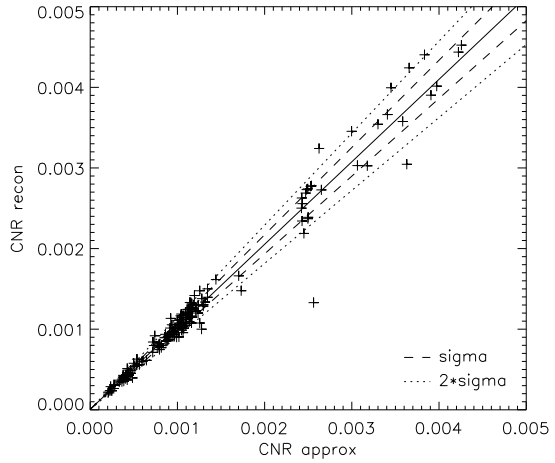

(a) All validation points

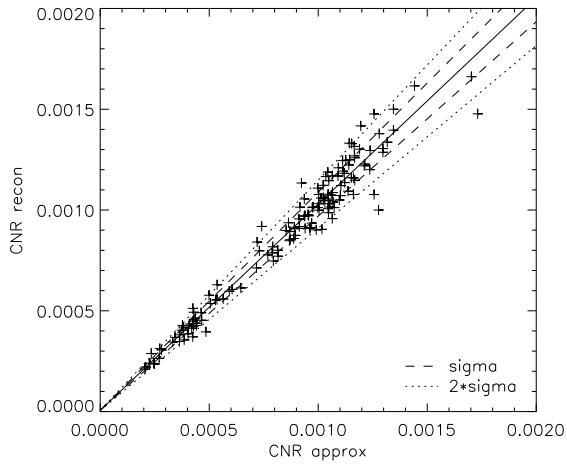

(b) Zoomed-in part of figure (a)

Fig. 6. Plot of the CNR calculated using the reference method versus the CNR obtained with the approximate method. (a) all validated designs, (b) a zoomed-in part of (a).

As shown in figure 6, the fitted line is slightly inclined towards the y-axis (slope 1.02, y-intercept $6.1*10^{-6}$), which means that the approximate method systematically underestimates the CNR a little. In addition, 49.4%, 82.8% and 95.4% of the points are located in the 68.3%, 95.4% and 99.7% confidence interval (one, two and three standard deviations), respectively. These results show that the new approximate method predicts successfully the reconstruction quality of a voxel.

V. Discussion

Although it has not been thoroughly tested yet, the reconstruction quality quantification method, presented in section II-B, should also be valid for multiple head multipinhole SPECT. In addition this method can be applied to PET and other SPECT applications as well.

Our method differs from the methods presented in [8]–[10] by the use of post-smoothed MLEM instead of MAP. However, if the regularization term $\beta \boldsymbol{U}$ is designed in such a way that $[\boldsymbol{F}+\beta \boldsymbol{U}]^{-1} = \boldsymbol{P}^j \boldsymbol{G}^j$, like in [15], the difference between MAP and post-smoothed MLEM fades away and equations (4) and (5) become equations (7) and (8). With our method we can easily impose a uniform target resolution, which has the advantage that different designs can be compared at the same resolution and that only one parameter has to be considered for optimization, i.e. the variance in the voxel of interest, or equivalently its CNR.

Some previously published methods, like [8], go even further in their approximations. They try to isolate shift-invariant factors, like the geometric projection matrix for positron emission tomography (PET) imaging. Since it is the same for all voxels, it only has to be calculated once. This saves a lot of computation time. For a pinhole system, however, it seemed impossible to distinguish and isolate shift-invariant factors. Another possibility is to isolate the matrices that are independent of the object, like the camera geometry matrix in [9], such that it is sufficient to calculate them in advance (just once). However, this is not useful for collimator design or for the examination of design parameters, since each camera geometry is only tested once. Therefore, we have been using the earlier stated approximations that are less efficient, but still much faster than the reference method. Nevertheless, calculating the impulse response and the covariance matrix, rather than only the CRC and the variance in the investigated voxel (as in [8], [9]), supplies extra - possibly useful - information. It might for example be interesting to know the exact shape of the impulse response or to see which points covariate heavily with the voxel of interest (e.g. to predict artifacts).

To discuss the performance of the suggested approximate method, we list the most time-consuming steps. For each examined voxel 1 projection, 1 backprojection, 1 3D Fourier transformation, 2 inverse 3D Fourier transformations and 2 3D convolutions (for post-smoothing) are required. It is obvious that the efficiency is much higher than that of the reference method, for which 152 post-smoothed MLEM reconstructions (2 of noise-free and 150 of noisy projection data) with 472 iterations (using relaxed ordered subsets) have to be executed for the first voxel and one more for each additional voxel. These 472 iterations used 61 main iterations (with a varying number of subsets), which require 61 forward and backward projections on the whole data set. As the main computational load is due to the forward and backward projections, the efficiency gain is about a factor 152*61 for the first point, and about a factor 61 for all next points. The time gain is thus huge if only a few points (up till several 100s) are under investigation. However, if one is interested in variance images of the complete phantom, a faster method, such as [19], is recommended.

Our approximation of the pseudoinverse $\mathbf{G}^j$ (in the Fourier domain) includes a factor $\max(\Re(\boldsymbol{F}^j), 0)$ both in the nominator and in the denominator. In our experience, frequencies with $\Re(\boldsymbol{F}^j) < 0$ have a negative influence on the accuracy and the stability of the approximations. This is probably because they are mostly caused by approximations and round-off errors, since the true Fisher information matrix is positive semidefinite.

To get a fixed resolution throughout the object, the post-smoothing filter was calculated for each voxel separately in this paper, since pinhole SPECT is shift-variant. For the reconstruction of real data, however, this is not practical. Though, since reconstruction near convergence is assumed, the difference in resolution between the voxels will be rather small after post-smoothing with a fixed filter.

If the software phantom is a centered homogeneous sphere, it is sufficient to investigate all voxels of a halfplane containing the rotation axis. Because of the circular symmetry of the reconstruction properties, this halfplane provides all information about the reconstruction of the entire sphere. For a central single pinhole or a multipinhole design that is symmetrical with respect to the central transaxial plane, a quarter plane (containing the rotation axis and the image center) is even sufficient. Of course, neighboring voxels are usually very alike, such that only a subset of voxels should be investigated. Furthermore, the less regular and homogeneous the software phantom, the more voxels should be examined.

From the validation studies we could remark that the CRC and the variance were more sensitive to the number of iterations (for the reference method) and to the choice of ϵ in equation (10) (for the approximate method) than the CNR. If too few iterations were performed or if ϵ was chosen too high, equations (7)-(10) became less accurate to approximate the CRC and the variance. Fortunately, an increase or decrease in CRC usually accords with an increase or decrease, respectively, in the variance, such that it has only a minor impact on the approximation of the CNR. This inaccuracy can be explained as follows: the higher the number of iterations, or equivalently, the smaller ϵ, the more high frequencies are included, which results in a better approximation of the pseudoinverse and a sharper impulse response. In that case, the large(r) amount of post-smoothing can more easily moderate small inaccuracies. For the same reason the inaccuracy also increases when enlarging the aperture diameter, since the resolution of the impulse response is already large with respect to the imposed target resolution. However, these pinhole diameters are not relevant for pinhole collimator design anyway, because the target resolution cannot be reached for these diameters.

The problem also becomes more complex if the shape of the impulse response resembles less an (isotropic) 3D-Gaussian. A possible solution to reduce this inaccuracy, is to allow more degrees of freedom to the post-smooth filter P^j, e.g. by allowing different FWHM in the three directions or by changing the shape of P^j. However, since the approximation of the CNR is acceptably accurate and in practice we post-

smooth with an isotropic Gaussian, we decided to proceed with the CNR (instead of the CRC and the variance) as the reconstruction image quality measure and with an isotropic Gaussian as post-smooth filter.

The target resolution might seem a little high at first sight, but from figure 3(b) it can be seen that the optimal pinhole diameter is only 1.5-1.8 mm. We preferred to keep the apertures large enough in order to guarantee sufficient sensitivity, as we are mainly interested in designs for low count rat brain studies.

VI. Future Work

In our simulations edge penetration was neglected. The effect of this approximation becomes increasingly important if the pinhole apertures get smaller, if the inclination angle becomes larger, and if the energy of photons emitted by the isotope used to image the phantom/animal gets higher. For the imaging of tracers labeled with ^{99m}Tc with pinhole apertures around 1.5 mm and acceptance angles around 60°, the effect of edge penetration on the relative performance of different designs is expected to be modest compared to the effect of varying the different pinhole design parameters considered in our study. Therefore, we presume that the global trends will remain the same, although e.g. a slight shift towards a lower optimal diameter might be expected, since the effective diameter is underestimated. In the future, we intend to extend our projection method with edge penetration modeling and to study its effect on the image quality.

The presented approximations will be used in the future to find a good design for rat brain imaging. Many different designs will be tested keeping the effects of the different design parameters in mind. The best design will be realized in practice and compared with our current 7-pinhole design (with aperture diameters of 1.5 mm, acceptance angles of 60°, a pinradius of 39 mm and a focal distance of 170 mm).

While searching for a better design, the following considerations should be kept in mind. Firstly, the image quality is shift- and object-variant. A well defined problem statement is the first step in the optimization process: for which application will the design be used, for which portion of the FOV should the quality be optimized, etc. Secondly, it still is an approximate method. Therefore it is useful to verify the quality of (some of) the best designs with the reference method. Finally, a trade-off is often necessary between the degree of quality improvement and the feasibility, or equivalently, the complexity of the design.

Another important issue is the positioning of the pinhole apertures in a multipinhole design. In this work we ignored the fact that regular patterns might cause artifacts in the reconstruction image in case of overlapping projections (see [5], [18], [25]) in the form of points (*ghost points*) or circular shapes (*ghost circles*). Positioning the apertures in an irregular pattern can help to reduce these artifacts. This was already observed in the 1970's [26], when one introduced the nonredundant arrays[6] to reduce the high correlations between different voxels. In the future we plan to have a closer look at the effect of these artifacts on the reconstruction image quality. It should be verified whether these artifacts are translated adequately into a lower CNR or whether they are only reflected in the covariance matrix of the reconstruction.

As mentioned during the discussion of the results in section IV, the overlapping projections do not only cause artifacts. They also influence the reconstruction image quality, since some projected activity cannot be linked one-to-one any more with a particular pinhole aperture. It is therefore not straightforward to value the extra sensitivity obtained by allowing projections to overlap. Using the method presented in this work, the influence of overlap is currently being studied. Preliminary results can be found in [27].

[6]In a nonredundant array one imposes that the displacement between every two pinholes appears once and only once.

VII. Conclusion

An accurate and efficient method is proposed to evaluate different single and multipinhole collimator designs for a particular application and a fixed target resolution. The quality of the reconstruction of each voxel can be quantified efficiently based on the contrast recovery coefficient of the linearized local impulse response and the variance. This method has been validated using post-smoothed MLEM reconstructions. The effect of changing a collimator design parameter, such as the aperture diameter, the focal distance or the number of pinholes, has been investigated.

References

[1] H. K. Tuy, "An inversion formula for cone-beam reconstruction." *SIAM J. Appl. Math.*, vol. 43(3), pp. 546-552, 1983.

[2] M. Ivanovic, D. A. Weber, and S. Loncaric, "Multi-pinhole collimator optimization for high resolution SPECT imaging." *IEEE Nucl. Sci. Symp. and Med. Imag. Conf. Rec.*, vol. 2, pp. 1097-1101, 1997.

[3] N. U. Schramm, G. Ebel, U. Engeland, T. Schurrat, M. Béhé, and T. M. Behr, "High-resolution SPECT using multipinhole collimation." *IEEE Trans. Nucl. Sci.*, vol. 50(3), pp. 315-320, 2003.

[4] M. F. Smith, S. R. Meikle, S. Majewski, and A. G. Weisenberger, "Design of multipinhole collimators for small animal SPECT." *IEEE Nucl. Sci. Symp. and Med. Imag. Conf. Rec.*, vol. 4, pp. 2291-2295, 2003.

[5] G. Bal, G. L. Zeng, R. M. Lewitt, Z. Cao, and P. D. Acton, "Study of different pinhole configurations for small animal tumor imaging." *IEEE Nucl. Sci. Symp. and Med. Imag. Conf. Rec.*, vol. 5, pp. 3133-3137, 2004.

[6] Z. Cao, G. Bal, R. Accorsi, and P. D. Acton, "Optimal number of pinholes in multi-pinhole SPECT for mouse brain imaging - a simulation study." *Phys. Med. Biol.*, vol. 50(19), pp. 4609-4624, 2005.

[7] J. A. Fessler and W. L. Rogers, "Spatial resolution properties of penalized-likelihood image reconstruction: space-invariant tomographs." *IEEE Trans. Image Proc.*, vol. 5(9), pp. 1346-1358, 1996.

[8] J. Qi and R. M. Leahy, "A theoretical study of the contrast recovery and variance of MAP reconstructions from PET data." *IEEE Trans. Med. Imag.*, vol. 18(4), pp. 293-305, 1999.

[9] J. Qi and R. M. Leahy, "Resolution and noise properties of MAP reconstruction for fully 3-D PET." *IEEE Trans. Med. Imag.*, vol. 19(5), pp. 493-506, 2000.

[10] L. J. Meng and D. K. Wehe, "Feasibility study of using hybrid collimation for nuclear environment imaging." *IEEE Trans. Nucl. Sci.*, vol. 50(4), pp. 1103-1110, 2003.

[11] L. J. Meng and N. H. Clinthorne, "A modified uniform Cramer-Rao bound for multiple pinhole aperture design." *IEEE Trans. Med. Imag.*, vol. 23(7), pp. 896-902, 2004.

[12] D. W. Wilson, B. M. W. Tsui, and H. H. Barrett, "Noise properties of the EM algorithm. II. Monte Carlo simulations." *Phys. Med. Biol.*, vol. 39(5), pp. 847-872, 1994.

[13] J. A. Fessler, "Mean and variance of implicitly defined biased estimators (such as penalized maximum likelihood): Applications to tomography." *IEEE Trans. Image Proc.*, vol. 5(3), pp. 493-506, 1996.

[14] J. A. Fessler and S. D. Booth, "Conjugate-gradient preconditioning methods for shift-variant image reconstruction." *IEEE Trans. Image Proc.*, vol. 8(5), pp. 688-699, 1999.

[15] J. W. Stayman and J. A. Fessler, "Compensation for nonuniform resolution using penalized-likelihood reconstruction in space-variant imaging systems." *IEEE Trans. Med. Imag.*, vol. 23(3), pp. 269-284, 2004.

[16] J. Nuyts and J. A. Fessler, "A penalized-likelihood image reconstruction method for emission tomography, compared to postsmoothed maximum-likelihood with matched spatial resolution." *IEEE Trans. Med. Imag.*, vol. 22(9), pp. 1042-1052, 2003.

[17] J. A. Fessler, "Analytical approach to regularization design for isotropic spatial resolution.", *IEEE Nuc. Sci. Symp. and Med. Imag. Conf. Rec.*, vol. 3, pp. 2022-2026, 2003.

[18] K. Vunckx, D. Bequé, M. Defrise, and J. Nuyts, "Single and multi-pinhole collimator design evaluation method for small animal SPECT." *IEEE Nucl. Sci. Symp. and Med. Imag. Conf. Rec.*, vol. 4, pp. 2223-2227, 2005.

[19] Y. Zhang-O'Connor and J. A. Fessler, "Fast predictions of variance images for fan-beam transmission tomography with quadratic regularization." *IEEE Trans. Med. Imag.*, vol. 26(3), pp. 335-346, 2007.

[20] L. S. Shepp and Y. Vardi, "Maximum likelihood reconstruction for emission tomography." *IEEE Trans. Med. Imag.*, vol. MI-1, pp. 113-122, 1982.

[21] M. H. Hudson and R. S. Larkin, "Accelerated image reconstruction using ordered subsets of projection data." *IEEE Trans. Med. Imag.*, vol. 13(4), pp. 601-609, 1994.

[22] C. Vanhove, M. Defrise, P. R. Franken, H. Everaert, F. Deconinck, and A. Bossuyt, "Interest of the ordered subsets expectation maximization (OS-EM) algorithm in pinhole single-photon emission tomography reconstruction: a phantom study." *Eur. J. Nucl. Med.*, vol. 27(2), pp. 140-146, 2000.

[23] E. Lauwers, D. Bequé, K. Van Laere, J. Nuyts, G. Bormans, L. Mortelmans, C. Casteels, L. Vercammen, O. Bockstael, B. Nuttin, Z. Debyser, and V. Baekelandt, "Non-invasive imaging of neuropathology in a rat model of alpha-synuclein overexpression." *Neurobiol. Aging*, vol. 28(2), pp. 248-257, 2007.

[24] J. A. Fessler, "Spatial resolution and noise tradeoffs in pinhole imaging system design: a density estimation approach." *Optics Express*, vol. 2(6), pp. 237-253, 1998.

[25] Y. Wang and B. M. W. Tsui, "Application of crosstalk concept to assessment of multi-pinhole collimator designs in small animal SPECT imaging." *IEEE Nucl. Sci. Symp. and Med. Imag. Conf. 2006, M16-8, San Diego, CA, USA*, 2006.

[26] M. J. E. Golay, "Point arrays having compact, nonredundant autocorrelations." *J. Opt. Soc. Am.*, vol. 61, pp. 272-273, 1971.

[27] K. Vunckx and J. Nuyts, "Effect of overlapping projections on reconstruction image quality in multipinhole SPECT." *IEEE Nucl. Sci. Symp. and Med. Imag. Conf. Rec.*, 2006.